# Asymmetry of the Distribution of Vertical Velocities of the Extratropical Atmosphere in Theory, Models, and Reanalysis

MATTHIEU KOHL[a] AND PAUL A. O'GORMAN[a]

[a] *Department of Earth, Atmospheric, and Planetary Sciences, Massachusetts Institute of Technology, Cambridge, Massachusetts*

ABSTRACT: The vertical velocity distribution in the atmosphere is asymmetric with stronger upward than downward motion. This asymmetry is important for the distribution of precipitation and its extremes and for an effective static stability that has been used to represent the effects of latent heating on extratropical eddies. Idealized GCM simulations show that the asymmetry increases as the climate warms, but current moist dynamical theories based around small-amplitude modes greatly overestimate the increase in asymmetry with warming found in the simulations. Here, we first analyze the changes in asymmetry with warming using numerical inversions of a moist quasigeostrophic omega equation applied to output from the idealized GCM. The inversions show that increases in the asymmetry with warming in the GCM simulations are primarily related to decreases in moist static stability on the left-hand side of the moist omega equation, whereas the dynamical forcing on the right-hand side of the omega equation is unskewed and contributes little to the asymmetry of the vertical velocity distribution. By contrast, increases in asymmetry with warming for small-amplitude modes are related to changes in both moist static stability and dynamical forcing leading to enhanced asymmetry in warm climates. We distill these insights into a toy model of the moist omega equation that is solved for a given moist static stability and wavenumber of the dynamical forcing. In comparison to modal theory, the toy model better reproduces the slow increase of the asymmetry with climate warming in the idealized GCM simulations and over the seasonal cycle from winter to summer in reanalysis.

SIGNIFICANCE STATEMENT: Upward velocities are stronger than downward velocities in the atmosphere, and this asymmetry is important for the distribution of precipitation because precipitation is linked to upward motion. An important and open question is what sets this asymmetry and how much it increases as the climate warms. Past work has shown that current theories greatly overestimate the increase in asymmetry with warming in idealized simulations. In this work, we develop a more complete theory and show that it is able to better reproduce the slow increase of the asymmetry with warming that is found over the seasonal cycle from winter to summer and in idealized simulations of warming climates.

## 1. Introduction

Many different meteorological variables—from geopotential height, to vorticity, to horizontal and vertical winds—show significant departures from Gaussianity in their climatology (Perron and Sura 2013). Understanding how these skewed distributions arise from some of the underlying physical asymmetries of the atmosphere (planetary rotation, uneven insolation, irreversible fall-out of particles during precipitation) is one of the fundamental challenges of dynamical meteorology. Our focus here is on the large-scale vertical velocity field which has stronger upward than downward motion (Perron and Sura 2013; Tamarin-Brodsky and Hadas 2019). We measure its asymmetry following O'Gorman (2011) by the factor

$$\lambda = \frac{\overline{\omega' \omega^{\uparrow\prime}}}{\overline{\omega'^2}}, \tag{1}$$

where $\omega^{\uparrow} = \omega$ for upward motion and $\omega^{\uparrow} = 0$ otherwise, and primes denote deviations from horizontal averages which are

denoted by an overbar. Assuming a vertical velocity distribution with zero mean, $\lambda = 0.5$ corresponds to upward and downward velocities that are of the same magnitude, and $\lambda \to 1$ corresponds to the limit in which upward motions are infinitely fast and occur over a vanishing ascent region.[1] The asymmetry parameter takes on typical values of $\lambda \approx 0.6$ in the midlatitudes, is larger in cyclones than anticyclones, and increases for storms over the seasonal cycle from winter to summer (O'Gorman 2011; Tamarin-Brodsky and Hadas 2019). The asymmetry of the vertical velocity distribution has been of key interest in studies of precipitation and its extremes (Sardeshmukh et al. 2015; Pendergrass and Gerber 2016) because the intensity of precipitation is closely associated with the strength of upward motion. Furthermore, a body of research on moist midlatitude dynamics has relied upon an effective static stability that depends on the

---

[1] If the mean $\omega$ is zero, then the asymmetry parameter $\lambda$ and the negative skewness $-\overline{\omega'^3}/(\overline{\omega'^2})^{3/2}$ increase together. However, $\lambda$ is used here because it is a lower-order statistic that tends to be more robust in calculations, because it is closely related to the updraft area fraction, and because it enters the moist effective static stability (cf. discussion in O'Gorman et al. 2018).

---

*Corresponding author*: Matthieu Kohl, mkohl@mit.edu

asymmetry parameter $\lambda$ to capture the modifying effects of latent heating on the circulation (O'Gorman 2011; Levine and Schneider 2015; Booth et al. 2015; Pfahl et al. 2015; Dwyer and O'Gorman 2017). While this effective static stability has proven a useful tool to convert dry into moist theories in a number of applications, it is not a closed theory since $\lambda$ is not known from theory and must be inferred from reanalysis or simulation data. One of the key problems is thus to understand what sets the value of the asymmetry and how it responds as the climate warms.

The variation of the asymmetry parameter with warming was investigated in a previous study by O'Gorman et al. (2018) using an idealized aquaplanet GCM in which large changes in climate and in the extent of the nonlinearity of the flow can be simulated relatively easily. While the asymmetry factor $\lambda$ increased strongly with warming for the most unstable modes of moist baroclinic instability, the asymmetry increased only slightly with warming in fully nonlinear simulations (O'Gorman et al. 2018, their Fig. 3b). This distinction is significant for our dynamical understanding since the atmosphere is in a macroturbulent state more akin to that of the fully nonlinear simulations, even if insights into cyclogenesis can be obtained from the study of unstable modes. Here, macroturbulence refers to the turbulence of large-scale eddies in the troposphere following Held (1999). We will refer to the small-amplitude unstable modes as the "modal regime" and the fully nonlinear simulations at statistical equilibrium as the "macroturbulent regime" from here on. The slight increase in $\lambda$ with warming in the macroturbulent regime of the idealized GCM over a wide range in climates is also consistent with what has been found for projected changes under the representative concentration pathway 8.5 emission scenario with the MPI-ESM-LR model (Tamarin-Brodsky and Hadas 2019).

In O'Gorman et al. (2018), the calculations of moist baroclinic instability differed from the fully nonlinear simulations by having small-amplitude disturbances but also by assuming that upward motion is saturated and by only taking into account moist diabatic tendencies from the large-scale condensation scheme and not from the moist convection scheme. To exclude the differences in the representation of moist processes as a cause for the different behavior of the asymmetry with warming, the authors performed a second set of simulations in which both large-scale condensation and moist convection schemes were turned off and the effects of latent heating were parameterized simply by reducing the dry static stability in the region of ascent by a factor $0 < r \leq 1$ in the spirit of simple moist dynamical theories (e.g., Emanuel et al. 1987; Zurita-Gotor 2005). Here, $r = 1$ corresponds to a fully dry simulation and $r \to 0$ corresponds to an increasingly warm and moist climate with weak moist static stability. The mean state of the simulations was held close to that of a control simulation by using a strong relaxation. From here on, we will refer to these simulations as "reduced stability simulations" to distinguish them from the "global warming simulations" that include convection and large-scale condensation schemes. Even with this greatly simplified representation of moist physics, a similar distinction between modal and macroturbulent

regimes emerged: as $r \to 0$, $\lambda$ in the modal regimes increases toward one corresponding to highly asymmetric vertical velocities, but $\lambda$ in the macroturbulent regime increases only slightly before equilibrating to a much lower value of about $\lambda = 0.71$ (O'Gorman et al. 2018, their Fig. 9). The different representation of moist physics are thus not a likely contributor to the different behavior of $\lambda$. Instead, the authors concluded that nonlinear equilibration to a macroturbulent state leads to a significant reduction of $\lambda$ compared to small-amplitude modes particularly in warm climates.

While simple theoretical scalings laws for the asymmetry of moist baroclinic waves exist (Emanuel et al. 1987; Zurita-Gotor 2005; Pendergrass and Gerber 2016), these do not carry over to the macroturbulent regime (O'Gorman et al. 2018, their Fig. 9), making it desirable to understand why modal theory fails and to develop a theory for the value of $\lambda$ that is reached in the macroturbulent regime.

To this end, in section 2 we place ourselves in the framework of moist quasigeostrophic (QG) theory and more specifically a moist QG omega equation in which the effects of latent heating are represented as an internal rather than external process. We show that the moist QG omega equation captures the behavior of $\lambda$ in the idealized GCM simulations of O'Gorman et al. (2018) when the dynamical forcing of vertical motion by the balanced motion is taken as given from the output of the idealized GCM. We go on to show that changes in $\lambda$ in the modal regime with warming or decreasing $r$ are related to changes in both the moist static stability and the dynamical forcing, while changes in $\lambda$ in the macroturbulent regime are primarily related to changes in moist static stability with the dynamical forcing not becoming very skewed. This leads to a smaller asymmetry in the macroturbulent phase compared with the modes for warm climates or at small values of $r$.

In section 3, we use a two-layer moist quasigeostrophic model to better understand the role of the moist static stability and dynamical forcing in setting $\lambda$. We show how a feedback between the dynamical forcing in the moist omega equation and the vertical velocity leads to an increase in asymmetry of the vertical velocity field in the modal regime. We then distill the insights from the macroturbulent inversions in section 2 into a simple toy model of the moist omega equation in the macroturbulent phase that is solved for a given moist static stability and wavenumber of the dynamical forcing. In contrast to moist baroclinic theory, we show that the toy model better reproduces the slow increase of the asymmetry with climate warming in the idealized GCM simulations.

In section 4, we apply moist baroclinic theory and our simple toy model to the change of asymmetry seen over the seasonal cycle in reanalysis. The seasonal cycle forms a useful test ground for asymmetry theories, since the moist static stability decreases a lot from winter to summer, particularly in the Northern Hemisphere. We show that while moist baroclinic theory overpredicts the increase in asymmetry from winter to summer, the toy model does better at capturing the slow change of the asymmetry seen over the seasonal cycle.

In section 5, we summarize our results and discuss future work.

## 2. Moist QG omega equation inversions applied to the idealized GCM simulations

The goal of this section is to understand the different sensitivity of $\lambda$ to warming between modal and macroturbulent regimes by applying a moist QG omega equation to the idealized GCM output from O'Gorman et al. (2018). The advantage of studying the vertical velocity through the framework of the moist omega equation rather than looking at the vertical velocity from the GCM output directly is that the moist QG omega equation allows us to tease apart the contributions to the vertical velocity and its asymmetry coming from dynamical forcing of vertical motion by the horizontal balanced flow versus thermodynamic contributions from the thermal stratification. The perspective of the moist omega equation then allows us to identify the causes of differences between $\lambda$ in the modal and macroturbulent regimes.

### a. The moist QG omega equation

The moist QG omega equation is written in pressure coordinates as

$$\nabla^2[\mathcal{R}(\omega)\sigma\omega] + f_0^2 \omega_{pp} = \text{Adv}. \tag{2}$$

A derivation is given in appendix A. Here, $\omega$ is the vertical velocity in pressure coordinates, $\nabla$ is the horizontal gradient, $f_0$ is the Coriolis parameter evaluated at the center of the domain used for the inversion, $\sigma = -[RT/(p\theta)]\theta_p$ is the static stability parameter with temperature $T$, potential temperature $\theta$, pressure $p$, and gas constant for dry air $R$, and the advective dynamical forcing of the moist omega equation is given by

$$\text{Adv} = -2\nabla \cdot \mathbf{Q} + f_0\beta\frac{\partial v_g}{\partial p}, \tag{3}$$

where $\beta$ is the meridional derivative of the Coriolis parameter, $\nabla$ is the horizontal gradient, and the Q vector is given by

$$\mathbf{Q} \equiv (Q_1, Q_2) = \left(-\frac{R}{p}\frac{\partial \mathbf{u}_g}{\partial x} \cdot \nabla T, \ -\frac{R}{p}\frac{\partial \mathbf{u}_g}{\partial y} \cdot \nabla T\right) \tag{4}$$

following the form in Holton (2004), where $\mathbf{u}_g \equiv (u_g, v_g)$ is the geostrophic wind vector. We have neglected the contributions from radiation and friction on the right-hand side of Eq. (2). The term related to the $\beta$ effect in Eq. (3) is generally small for synoptic motions such that the forcing of ascending and descending motions by the adiabatic flow is determined largely by the convergence and divergence of the Q vector, which compactly captures the effects of advection of temperature perturbations by the geostrophic motion on an isobaric surface (Holton 2004).

The static stability reduction factor $\mathcal{R}(\omega)$ is given by

$$\mathcal{R}(\omega) = \begin{cases} r, & \omega \le 0, \\ 1, & \omega < 0, \end{cases} \tag{5}$$

where $r$ is given by

$$r = \frac{\theta \ \Gamma_m}{\theta^* \ \Gamma_d}\frac{\dfrac{\partial \theta^*}{\partial p}}{\dfrac{\partial \theta}{\partial p}}, \tag{6}$$

under the assumption of saturated moist-adiabatic ascent [see Eq. (7) of Fantini 1995]. Here, $\theta^*$ is the saturated equivalent potential temperature, $\Gamma_m$ is the moist adiabatic lapse rate and $\Gamma_d$ is the dry adiabatic lapse rate. The nonlinear character of the $\mathcal{R}(\omega)$ factor expresses the fundamental asymmetry that is introduced by considering the effects of moisture on the dynamics: while the ascending air is assumed saturated, releases latent heat upon condensation, and feels a reduced static stability, the descending air is subsaturated after irreversible fallout of condensate during precipitation and feels the full static stability. This parameterization has been used in theoretical studies with semigeostrophic equations in Emanuel et al. (1987) and subsequently with quasigeostrophic equations (Fantini 1995; Zurita-Gotor 2005; Kohl and O'Gorman 2022) to study the modifying effects of latent heating on canonical dynamical examples such as baroclinic waves and fronts. The reduction factor $r$ calculated from Eq. (6) is a strong function of the vertical coordinate and approaches values of 1 in the upper troposphere (Whitaker and Davis 1994). At 500 hPa typical values of $r$ in the Northern Hemisphere range between $r = 0.4$ in winter and $r = 0.1$ in summer (see Fig. 9). We refer to the product $\mathcal{R}\sigma = r\sigma$ in updrafts as the moist static stability, and to Adv as the advective or dynamical forcing of the moist omega equation. Applying the inversion to both the most unstable modes and macroturbulent state of the idealized GCM simulations allows us to assess the magnitude of the contributions from the moist static stability and dynamical forcing to the asymmetry parameter and to identify which contribution is weaker in the macroturbulent regime leading to a reduced asymmetry compared with the modal regime.

### b. Details of the idealized GCM simulations

We briefly describe the GCM and simulations to which the moist omega equation is applied here but further details can be found in O'Gorman et al. (2018). The idealized GCM is based on a spectral version of the Geophysical Fluid Dynamics Laboratory (GFDL) atmospheric dynamical core (see Frierson et al. 2006; Frierson 2007; O'Gorman and Schneider 2008). The resolution is T85 with 30 vertical levels, and this resolution is used for both the global warming and reduced stability simulations. A thermodynamic mixed layer ocean of depth 0.5 m forms the lower boundary condition and no horizontal ocean heat transport or sea ice is included. Moist convection is parameterized using the scheme of Frierson (2007). Longwave radiation is modeled using a two-stream gray scheme. There are no seasonal or diurnal cycles of shortwave radiation and no cloud or water vapor radiative effects.

For the global warming simulations, the climate is varied by multiplying the longwave optical thickness by a factor $\alpha$, where $\alpha = 1.0$ corresponds to the control climate with global mean surface temperature of 288 K. The simulations were run for a period of 300 days after spinup. The most unstable modes were calculated through repeated rescaling of perturbations to small amplitude, assuming upward motion to be saturated, for a

period of 300 days and using a basic state equal to the zonal and time mean of a fully nonlinear simulation for that climate (but with mean meridional and vertical winds set to zero). We emphasize that these instability calculations are hence different from baroclinic life cycle experiments, in which perturbations are not periodically rescaled to keep them at small amplitude.

For the reduced stability simulations, latent heating was parameterized by reducing the static stability in ascending air, and the radiation, large-scale condensation and moist convection schemes were turned off. The reduction factor $r$ in ascending air was specified as a constant in the troposphere and smoothly transitioned as a function of pressure to a value of one in the stratosphere following the vertical profile $r + 0.5(1 - r)\{1 - \tanh[(p - p_u)/p_w]\}$, where $p_u = 200$ hPa is the nominal uppermost pressure level for the reduction in static stability, and $p_w = 50$ hPa is the width of the transition region about this level (O'Gorman et al. 2018). Hence, the reduction factor $r$ no longer follows Eq. (6) in the reduced stability simulations. The mean state of the simulations was held close to that of the control simulation ($\alpha = 1.0$) by using a strong relaxation. The simulations were run for 300 days after spinup. The most unstable mode was calculated under the reduced stability parameterization following the same small-amplitude approach as was used for the global warming simulations.

### c. Methods: Numerical approach to inverting the moist omega equation

We use the output from the idealized GCM simulations of O'Gorman et al. (2018) for the moist static stability and the dynamical forcing at every time step to invert Eq. (2) for $\omega$, thus leaving the time evolution of the flow to the higher-order dynamics of the GCM. The nonlinearity in latent heating enters through the factor $\mathcal{R}(\omega)$ which depends on the reduction factor $r$ in regions of ascent. For the global warming simulations, $r$ is calculated from the temperature and pressure fields using Eq. (6) and varies horizontally, vertically, and in time. As the climate warms, $r$ gets smaller because the thermal stratification in the midlatitudes approaches a moist adiabat. At each vertical level, we set $r = 0$ if $r < 0$ and $r = 1$ if $r > 1$ to ensure the inversions are well posed. For the reduced stability simulations, we simply use the specified $r$ profile that had been used in those simulations (see section 2b above).

The moist quasigeostrophic omega equation [Eq. (2)] has been solved before in the context of small-amplitude baroclinic modes in a quasigeostrophic model (Fantini 1995). Here, we go further and solve the moist omega equation on the sphere using output from a GCM both in the regime of small-amplitude modes and fully macroturbulent flows. The domain spans latitudes 25°–65° with Dirichlet boundary conditions $\omega = 0$ on all boundaries, except at the lower boundary where we use $\omega = \omega_{GCM}$, with $\omega_{GCM}$ the vertical velocity taken from the idealized GCM at each time step. Solving Eq. (2) is a difficult task due to the nonlinearity of $\mathcal{R}(\omega)$ which represents latent heating as an internal part of the dynamics rather than as an external forcing in the dry omega equation. We solve the equation iteratively as

$$\nabla^2[\sigma(p)\omega^{n+1}] + f_0^2 \omega_{pp}^{n+1} = \text{Adv} + \nabla^2\{[1 - \mathcal{R}(\omega^n)]\sigma(p)\omega^n\},$$

(7)

where $\omega^n$ is the solution at iteration $n$. The iterative scheme behind Eq. (7) has been written in such a way as to suggest a similarity to the repeated application of an omega equation with explicit heating term $-(\kappa/p)\nabla^2 J = \nabla^2\{[1 - \mathcal{R}(\omega^n)]\sigma\omega^n\}$ on the right-hand side, where $J$ is the latent heating, and $\kappa$ is the ratio of the gas constant to specific heat capacity at constant pressure [see also Eq. (A1)]. We have found that this form improves convergence of the inversions. We start with the dry solution obtained for $\mathcal{R}(\omega) = 1$ everywhere as an initial guess. At each iteration step, the equation is inverted using a 3D variant (Zedan and Schneider 1983; Ferziger and Perić 2002) of the strongly implicit method (Stone 1968). We continue iterating until $\text{rms}(\omega^{n+1} - \omega^n)/\text{rms}(\omega^{n+1}) \leq 10^{-3}$.

While $\sigma$ can in general be a function of the horizontal and vertical, we have found it useful for numerical stability to average $T$ and $\theta$ horizontally before calculating $\sigma$. Hence, the background stratification that enters Eq. (2) for our inversions does not vary in the horizontal, although it is recalculated for each time step and so can vary in time. Because the moist static stability is a product of $\mathcal{R}(\omega)\sigma(p)$, and $\omega$ is a three-dimensional field (as is $r$ for the global warming simulations), the moist static stability will also remain a three-dimensional field.

Horizontal winds, vertical velocity, and temperature from the GCM output were interpolated from sigma to pressure coordinates and replaced with NaN wherever the interpolated pressure was below the surface pressure. The pressure levels span from 989 to 3 hPa. The lower boundary condition was imposed at the lowest pressure level where no NaN values were encountered in the domain at each instant in time, which is typically 928 hPa. The geostrophic component of the wind was calculated as the rotational part of the full horizontal wind field, to minimize the influence of gravity waves (Nielsen-Gammon and Gold 2008), by inverting the relative vorticity on a global spherical grid in pressure coordinates.

Inversions with random initial guesses were also tried and the solutions were found to be insensitive to the choice of initial guess but take longer to converge. We have found it necessary to include $\omega = \omega_{GCM}$ as the lower boundary condition to better capture the macroturbulent values of $\lambda$ in the global warming simulations, which were underestimated with the simpler boundary condition $\omega = 0$. We use the same lower boundary condition for the modal inversions and for the macroturbulent inversions in the reduced stability simulations for consistency, even though it did not substantially improve the agreement in these cases. Stricter convergence criteria $\text{rms} < 10^{-4}$ have also been experimented with but the solutions and values of $\lambda$ were visually indistinguishable. Although the GCM domain is periodic in the zonal direction, the $\omega = 0$ boundary condition in the zonal direction has been adopted for implementational simplicity since the
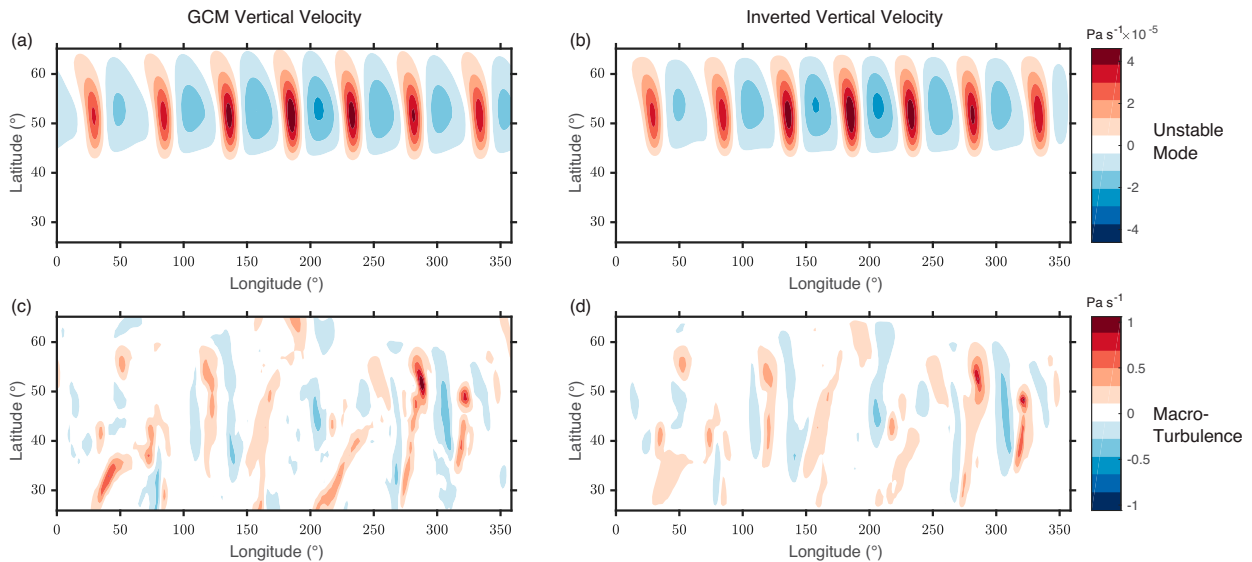
FIG. 1. Comparison of the instantaneous GCM vertical velocity field ($-\omega$; red indicates upward motion) to the inverted vertical velocity field obtained from inversion of Eq. (2), at 500 hPa. Results are shown for (a),(b) the unstable mode and (c),(d) the macroturbulent regime of the global warming simulations of O'Gorman et al. (2018) at a global-mean surface air temperature of 288 K. The modes were calculated by O'Gorman et al. (2018) through repeated rescaling of the equations to small amplitude, and hence, their magnitude is arbitrary. The time instant chosen for comparison was arbitrary.

solver was developed from a preexisting code with Dirichlet boundary conditions used in Li and O'Gorman (2020). Since we are interested in the statistics of $\lambda$ and are considering averages over a large domain, the statistics are expected to be insensitive to what happens near the horizontal boundaries. The goodness of the agreement between the inverted and GCM vertical velocities and their asymmetry $\lambda$ calculated over the domain (see section 2d) give us confidence that the periodic boundary effects can be neglected for the purpose of this study.

### d. Results of the inversions

We begin by comparing the GCM and inverted vertical velocity field at 500 hPa for the most unstable mode and macroturbulence regime of the global warming simulation at a global-mean surface air temperature of 288 K (the reference simulation that is most similar to the current climate) at a single instant in time. A midtroposphere level is chosen because that is roughly where the vertical velocity is strongest. Two-dimensional fields are shown in Fig. 1 and cross sections at 50°N latitude in Fig. 2. Focusing on the modes, we observe that inverted and GCM vertical velocity field are in near perfect agreement, except close to the boundaries where a different boundary condition was implemented (see edges of the domain in Fig. 2a). Focusing on the macroturbulent fields, we observe that the agreement between inverted and GCM vertical velocity field is less good, and this is as expected since the GCM flow is in a larger Rossby number state and does not assume upward motion to be saturated. Nevertheless, the inverted vertical velocity is able to capture most of the large-scale ascent and descent patterns well, as confirmed by the

cross section shown in Fig. 2b.[2] Similar results were found in the reduced stability simulations (not shown).

We now compare the statistics of the asymmetry parameter $\lambda$ for inverted and GCM vertical velocities in both the reduced stability and global warming simulations (Fig. 3). The value of $\lambda$ was calculated between 40° and 60° latitude for the global warming simulations and between 25° and 65° in the reduced stability simulations and then averaged in time, meridionally over the latitude band and vertically over the troposphere. Following O'Gorman et al. (2018), a wider latitude band is chosen for the reduced stability simulations because the unstable modes are not necessarily localized in the 40°–60° latitude band in this case. The tropopause was defined as the highest level at which the domain (40°–60° latitude band) and time mean lapse rate is greater than 2 K km$^{-1}$. To facilitate comparison between the global warming and reduced-stability simulations, Fig. 4 shows the reduction factor $r$, calculated from Eq. (6), versus global mean surface temperature in the global warming simulations at 500 hPa and averaged vertically up to the tropopause. The reduction factor $r$ decreases as the climate warms and the midlatitude stratification approaches moist adiabatic.

The basic behavior of the idealized simulations that we are trying to capture and understand is that in response to increasing global-surface temperature or decreasing reduction

---

[2] For inversions in the reference climate shown here, it is frequently the case that the inversion underestimates the strongest updrafts, even when the full horizontal winds, rather than the geostrophic winds, are used in the inversion. However, in warmer climates this is no longer the case and the inversion can overestimate the peak updraft strength. This is consistent with the overprediction in asymmetry in warmer climates in Fig. 3.
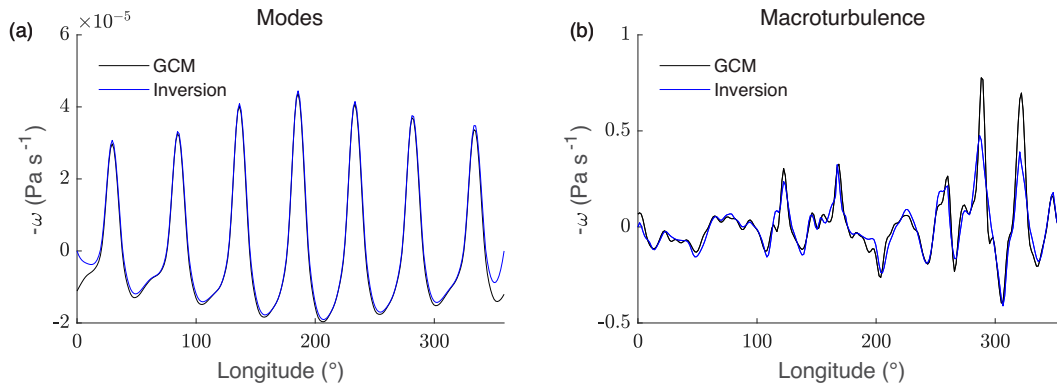
FIG. 2. Cross section of the GCM (black) and inverted (blue) vertical velocity fields shown in Fig. 1 at latitude 50° for (a) the mode and (b) the macroturbulent regime. The amplitude of the mode is arbitrary. Please note that instead of periodic boundary conditions used in the zonal direction in the GCM, Dirichlet conditions with $\omega = 0$ have been used in the inversions, and hence, agreement is not expected at the boundaries (see further discussion in section 2c).

factor $r$, $\lambda$ increases strongly for the most unstable modes but increases only moderately in the macroturbulent regime (Figs. 3a,c; solid red vs solid blue line). We first discuss results for full inversions that include latent heating through $\mathcal{R}(\omega)$, and thus, the asymmetry can result from both latent heating and the dynamical forcing. These results confirm that the moist QG omega equation is able to capture the behavior of $\lambda$ in the idealized GCM. We then discuss inversions in which we artificially set $\mathcal{R}(\omega) = 1$, and hence, the asymmetry in the inverted vertical velocity must only come from the dynamical forcing. These results allow us to separate the contributions to the asymmetry coming from only the dynamical forcing versus those coming from both the moist static stability and the dynamical forcing.

We focus first on the results of the full inversion that includes latent heating through $\mathcal{R}(\omega)$ (Figs. 3a,c). We see that $\lambda$ of the inverted vertical velocity field (which we will refer to as QG $\lambda$) is in close to perfect agreement with $\lambda$ of the GCM vertical velocity field for the modes in both types of simulations. For the macroturbulent regime, QG and GCM $\lambda$ are in reasonably good agreement, with QG $\lambda$ becoming larger than the GCM $\lambda$ at low values of $r$ and high global-mean surface air temperatures. In the dry limit of $r = 1$, $\lambda = 0.5$ for the modes indicating a symmetric vertical velocity distribution, whereas $\lambda$ is slightly greater than 0.5 for the macroturbulent regimes, indicating that even a dry flow has up–down asymmetry at finite amplitude (cf. discussion in O'Gorman et al. 2018). Despite the limitations in applying the QG omega equation to finite-amplitude flows with a simplified representation of moist physics, we conclude that the QG omega equation is able to capture the different behavior of $\lambda$ between unstable modes and macroturbulence in the idealized GCM.

Focusing next on the inversions in which $\mathcal{R}(\omega) = 1$ (Figs. 3b,d), which isolates the effects of the dynamical forcing, we see that while the vertical velocity field remains asymmetric in the modal regime, the vertical velocity field is close to symmetric in the macroturbulent regime in both types of simulations. For the macroturbulent regime (blue dashed curve) $\lambda$ is close to 0.55 for all values of $r$, while for the modal regime (red dashed

curve) it increases to peak values of 0.8. This difference in $\lambda$ between modal and macroturbulent regimes becomes more pronounced in the limit of high temperature or low values of $r$. For example, for small values of $r$ in the reduced stability simulations, we find $\lambda \sim 0.80$ for the modes versus $\lambda \sim 0.56$ in the macroturbulent regime. The lack of contribution to $\lambda$ from the dynamical forcing in the macroturbulent regime is consistent with the behavior of the dynamical forcing: the value of the vertically averaged skewness over the troposphere of $-\mathrm{Adv}$ is 0.1 in the macroturbulent phase for $r = 0.01$, compared to 5.9 in the modal phase at $r = 0.01$. We conclude that while both $\mathcal{R}(\omega)$ and dynamical forcing contribute to the asymmetry of the vertical velocity distribution in the modal phase leading to large asymmetries, $\mathcal{R}(\omega)$ is the primary contributor to the asymmetry of the vertical velocity distribution in the macroturbulent phase and the dynamical forcing does not contribute much leading to substantially reduced asymmetries.

## 3. Understanding asymmetry behavior using two-layer moist QG

We next use a two-layer moist QG framework to better understand the asymmetry behavior in the modal and macroturbulent regimes. We begin by developing an understanding for why the dynamical forcing is skewed in the modal regime in section 3a, before distilling the insights of the 3D inversions into a toy model for $\lambda$ in the macroturbulent regime in section 3b.

The two-layer moist QG equations on an $f$ plane with layers of equal thickness take the nondimensional form

$$\partial_t \nabla^2 \phi + J(\phi, \nabla^2 \phi) + J(\tau, \nabla^2 \tau) = 0, \tag{8}$$

$$\partial_t \nabla^2 \tau + J(\phi, \nabla^2 \tau) + J(\tau, \nabla^2 \phi) + w = 0, \tag{9}$$

$$\partial_t \tau + J(\phi, \tau) + \mathcal{R}(w)w = 0, \tag{10}$$

with barotropic and baroclinic streamfunction $\phi = (\psi_1 + \psi_2)/2$ and $\tau = (\psi_1 - \psi_2)/2$, where $\psi_1$ refers to the streamfunction in
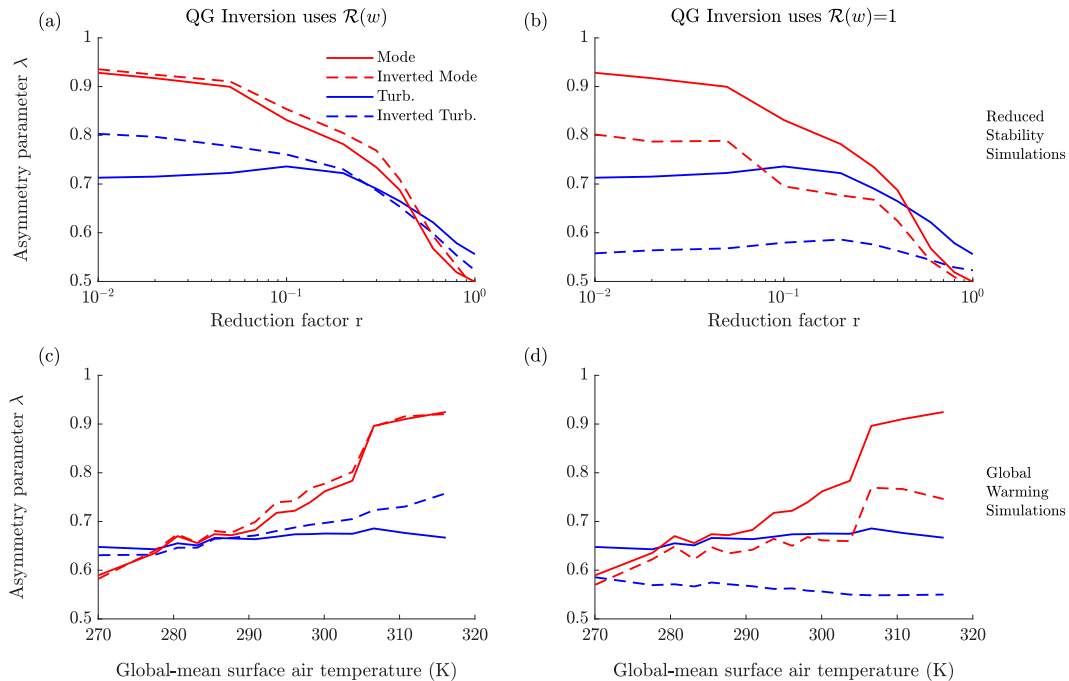
FIG. 3. Comparison of the asymmetry parameter $\lambda$ for GCM vertical velocities (solid lines) and the QG inverted vertical velocities calculated from the inversion of Eq. (2) (dashed lines). Results are shown for the modal (red) and macroturbulent (blue) regimes in the (a),(b) reduced stability simulations and (c),(d) global warming simulations from O'Gorman et al. (2018). In (a) and (c) $\mathcal{R}(\omega)$ was used in the inversion of Eq. (2), whereas in (b) and (d) $\mathcal{R}(\omega) = 1$ was used in the inversions. Hence, in (a) and (c) the asymmetry of the vertical velocity distribution comes from both $\mathcal{R}(\omega)$ and the dynamical forcing (Adv), whereas in (b) and (d) the asymmetry only comes from the dynamical forcing. $\lambda$ was calculated between 40° and 60° latitude for the global warming simulations and between 25° and 65° latitude in the reduced stability simulations and then averaged in time and vertically over the troposphere.

the upper layer and $\psi_2$ to the streamfunction in the lower layer, and with Jacobian $J(A, B) = A_x B_y - A_y B_x$. These equations are obtained from Eqs. (A6)–(A8) in Kohl and O'Gorman (2022) after setting the boundaries at top and bottom to be horizontal $h_1 = h_2 = 0$ and neglecting the radiative cooling term. The equations have been nondimensionalized assuming an advective time scale and with the deformation radius $L_D = NH/(\sqrt{2}f)$ as the horizontal length scale where $H$ is the layer height.[3] The $\beta$ effect is neglected here for simplicity and because we found in the idealized GCM simulations that the term containing $\beta$ on the right-hand side of the full 3D moist omega equation Eq. (2) is generally an order of magnitude smaller than the Q-vector term. Equations (8) and (9) describe the advection of barotropic and baroclinic vorticity, and Eq. (10) represents the thermodynamic equation with $\mathcal{R}(\omega)$ and $w$ defined midway between the upper and lower layers. The nonlinear term $\mathcal{R}(\omega)$, as before, encapsulates the effects of latent heating through a reduction of static stability in updrafts but not downdrafts due to the irreversibility introduced upon fallout of condensate during precipitation.

---

[3] Discretizing the continuous thermodynamic equation leads to a deformation radius involving $N$ at the midtropospheric level rather than a reduced gravity.

### a. Behavior of the dynamical forcing for moist unstable modes

To study the asymmetry of the vertical velocity in the limit of small-amplitude perturbations growing on a basic state, we linearize the advective terms of the two-layer moist QG equations around a zonally uniform basic shear state in thermal wind balance $\tau_0 = -y$, $\phi_0 = 0$, $w_0 = 0$. We also assume the perturbations to be independent of the $y$ direction. This yields the equations

$$\partial_t \phi_{xx} + \tau_{xxx} = 0, \qquad (11)$$

$$\partial_t \tau_{xx} + \phi_{xxx} + w = 0, \qquad (12)$$

$$\partial_t \tau - \phi_x + \mathcal{R}(w)w = 0, \qquad (13)$$

where $\tau$, $\phi$, and $w$ now refer to small-amplitude perturbations about the basic state.

Equations (11)–(13) have been studied in quasigeostrophic (Zurita-Gotor 2005) and semigeostrophic (Emanuel et al. 1987) form to analyze the effects of latent heating on the growth rate and length scale of the most unstable modes of baroclinic instability. It was found that latent heating increases the growth rate and shifts the most unstable mode to
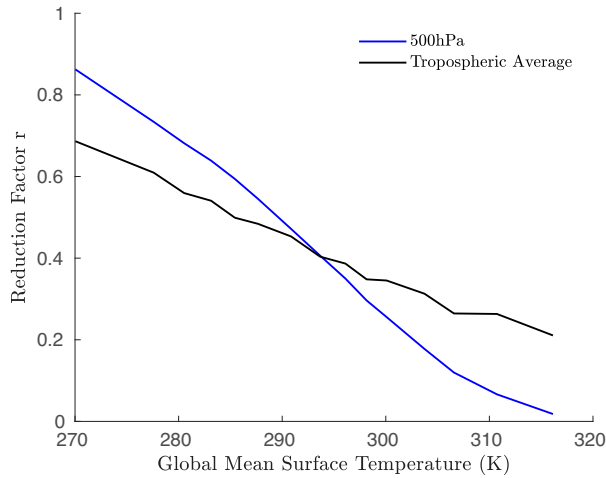
FIG. 4. Reduced stability parameter $r$ vs global mean surface temperature in the idealized global warming simulations. The $r$ value was calculated using Eq. (6) and is shown both at 500 hPa (blue line) and averaged vertically up to the tropopause (black line). The tropopause was defined as the highest level at which the domain (40°–60° latitude band) and time mean lapse rate for a given climate simulation is greater than $2 \text{ K km}^{-1}$.

smaller length scales. Here, we focus on the effect of latent heating on the asymmetry of the vertical velocity of the most unstable moist modes.

### 1) METHODS: CALCULATION OF MOST UNSTABLE MODE IN TWO-LAYER MODEL

To calculate the fastest growing modes for a given static-stability reduction factor $0 \le r \le 1$, we solve Eqs. (11)–(13) numerically. To this end, we discretize the equations using second-order central finite differences in a periodic domain in $x$ of size $L = 8\pi$ with grid spacing $\Delta x = 0.13$. The equations are solved using the same procedure as outlined in Kohl and O'Gorman (2022) but noting that here we do not tilt the upper and lower boundaries. We refer the reader to the paper for more detail and only summarize the basics here. The barotropic and baroclinic vorticity equations [Eqs. (11) and (12)] are integrated forward in time and the system of equations is closed by calculating the vertical velocity $w$ at each time step from the nonlinear omega equation,

$$[\mathcal{R}(w)w]_{xx} - w = 2\phi_{xxx}, \qquad (14)$$

which is formed by eliminating the time derivatives between Eqs. (12) and (13). Here $2\phi_{xxx}$ is the dynamical forcing Adv for the small-amplitude two-layer model. The dynamical fields are rescaled whenever a threshold rms $(\mathbf{x}) > 10$ (where $\mathbf{x} = [\tau_{xx}, \phi_{xx}]$) is reached to avoid large numbers, which could cause problems with the numerical representations, and the equations are run forward in time until the solution has converged to a normal mode [see Kohl and O'Gorman (2022) for further details].

### 2) RESULTS

An example vertical velocity profile of the most unstable moist mode in this system at $r = 0.1$ is shown in Fig. 5a. The solution consists of a periodic wave whose ascent length is reduced compared to the descent length. This is consistent with the structure of the most unstable mode that was found in the idealized GCM calculations (see Fig. 2a).

We repeat the calculation for different values of $r$ and compare the asymmetry of the most unstable mode in this two-layer system to the asymmetry for the modes of the reduced stability GCM simulations (see Fig. 5b). The reduced stability simulations are chosen for ease of comparison to our two-layer model, since a constant reduction factor is applied throughout the troposphere in these simulations. In the global warming simulations, $r$ varies with altitude which is more difficult to capture in a two-layer setting. Because the vertical velocity field is a function of $x$ only, we will refer to the predictions of this two-layer moist QG model in the small-amplitude regime as 1D modal theory (to be distinguished from the 1D toy model for the macroturbulent phase introduced in the next section).

Looking at Fig. 5b, we see that the asymmetry of the most unstable modes of the 1D theory agrees remarkably well with that found in the idealized GCM experiments given the simplicity of the two-layer setup. The modes become very skewed as $r \to 0$, which can also be confirmed by looking at the $w$ profile of the most unstable mode from the 1D theory at $r = 0.1$ (Fig. 5a). The ascent length is greatly reduced compared to the descent length, in line with the results of Emanuel et al. (1987) and Zurita-Gotor (2005). Adv is markedly skewed in the two-layer theory with a skewness of $-2.1$, where the skewness is calculated as $-\overline{\text{Adv}'^3}/(\overline{\text{Adv}'^2})^{3/2}$. Physically, $\text{Adv} = 2\phi_{xxx}$ is the zonal advection of barotropic vorticity. While the streamfunction $\phi$ and barotropic vorticity $\phi_{xx}$ remain close to unskewed, the zonal advection of barotropic vorticity nonetheless becomes very skewed.

We can now use the two-layer moist QG framework to explain why Adv of the moist omega equation imparts so much asymmetry during the modal regime, as was also found for the idealized GCM simulations in section 2d. Combining Eqs. (11) and (12), it is possible to write an explicit equation for $\text{Adv} = 2\phi_{xxx}$ of the moist omega equation in the modal regime

$$\partial_{tt} 2\phi_{xxx} = (2\phi_{xxx})_{xx} + 2w_{xx}, \qquad (15)$$

which forms a complete set of equations when combined with the moist omega equation [Eq. (14)]. We consider an initial value problem which is solved in time until the solution converges to a mode starting from initial conditions in which Adv is unskewed. We observe from Eq. (15) that Adv satisfies a wave equation in the modal regime with $2w_{xx}$ as its source term. When the atmosphere is dry ($r = 1$) and Adv is the same magnitude in ascending and descending regions, then $2w_{xx}$ is also of the same magnitude in ascending and descending regions by Eq. (14). If Adv is unskewed initially, it will
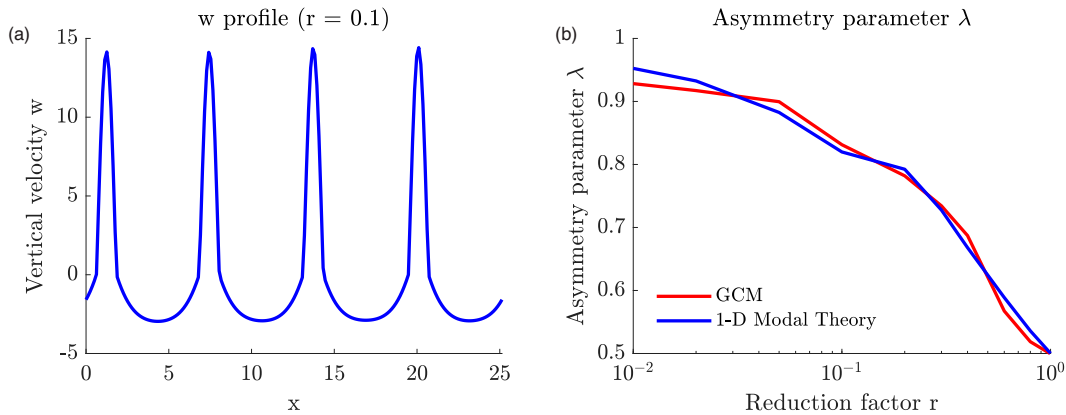
FIG. 5. (a) Vertical velocity profile of the most unstable mode of 1D moist baroclinic theory at $r = 0.1$. (b) Comparison of the asymmetry parameter $\lambda$ for the most unstable modes predicted by 1D moist baroclinic theory, and for the most unstable modes calculated using a reduced stability parameterization for the GCM simulations of O'Gorman et al. (2018). The $\lambda$ of the modes in the reduced stability GCM simulations is averaged over the troposphere and was also shown in Fig. 3a.

thus remain so in time by [Eqs. (14), (15)].[4] However, when the atmosphere is moist and thus $r < 1$, the moist omega equation implies that $w_{xx}$ becomes different in magnitude between ascending and descending regions even if Adv is unskewed. An example of a $w$ profile in this situation is given by solutions to the moist omega equation with an unskewed Adv that will be considered in the next section (see Fig. 6a). For brevity, from now on we will refer to the extent to which $w_{xx}$ is greater in magnitude in the ascent region compared to the descent region as the asymmetry of $w_{xx}$, and similarly for the asymmetry of Adv. By Eq. (15) the asymmetry of $w_{xx}$ is imparted to Adv such that Adv also becomes more asymmetric. The smaller $r$, the more asymmetric $w_{xx}$ and hence Adv, which explains the increased asymmetry imparted to the vertical velocity by Adv in warm climates or for low values of $r$ in section 2. Since Adv forces the omega equation, its asymmetry will be imparted to the asymmetry of $w$ and hence also that of $w_{xx}$. A feedback is established. For an initial value problem starting with a symmetric Adv, the asymmetry of the Adv is thus expected to grow through the feedback mechanism before equilibrating to a constant value eventually when the modal structure is reached and all terms in Eq. (15) grow exponentially at the same rate.

### b. Toy model for moist macroturbulence

In the macroturbulent phase, the full nonlinearities in Eqs. (8)–(10) are retained and the moist QG omega equation is instead given by

$$\nabla^2[\mathcal{R}(w)w] - w = 2J(\tau, \nabla^2\phi) - 2J(\phi_x, \tau_x) - 2J(\phi_y, \tau_y), \quad (16)$$

which can be derived by eliminating time derivatives in Eqs. (9) and (10). It is hard to make any general theoretical statements about the right-hand side of this equation given the macroturbulent nature of the flow. Unlike in modal theory, scrambling by the nonlinear advective terms means that a simple amplifying feedback between the asymmetry of Adv and $w$ is no longer expected, and this is supported empirically by both the inversions for the reduced stability and global warming simulations which showed that Adv was unskewed and made only small contributions to the asymmetry of the vertical velocity distribution. Motivated by this result, we study a simple 1D toy model of the moist two-layer QG omega equation in the macroturbulent phase given by

$$[\mathcal{R}(w)w]_{xx} - w = \sin(kx), \quad (17)$$

with the dynamical forcing on the right-hand side described by an unskewed sinusoidal function with nondimensional wavenumber $k$. The sinusoid function is chosen as a simple representation of an unskewed dynamical forcing. The wavenumber $k$ is introduced to represent the physical dependence of the moist omega equation on the scale of the dynamical forcing. Since we currently do not have a theory for the power spectrum of Adv, the wavenumber $k$ is taken here as an externally imposed parameter in addition to the reduction factor $r$. Although the sinusoidal forcing is clearly a gross simplification of the true dynamical forcing, we argue that it is nonetheless useful to illustrate some of the controls on $\lambda$ implied by the moist omega equation with an unskewed dynamical forcing at different length scales.

#### 1) METHODS: SOLUTION OF THE TOY MODEL AND DIAGNOSIS OF $K$

We invert Eq. (17) numerically for a given wavenumber $k$ and reduction factor $r$ on a domain of length $L = 2\pi/k$ using 300 evenly spaced grid points. The solution technique for the
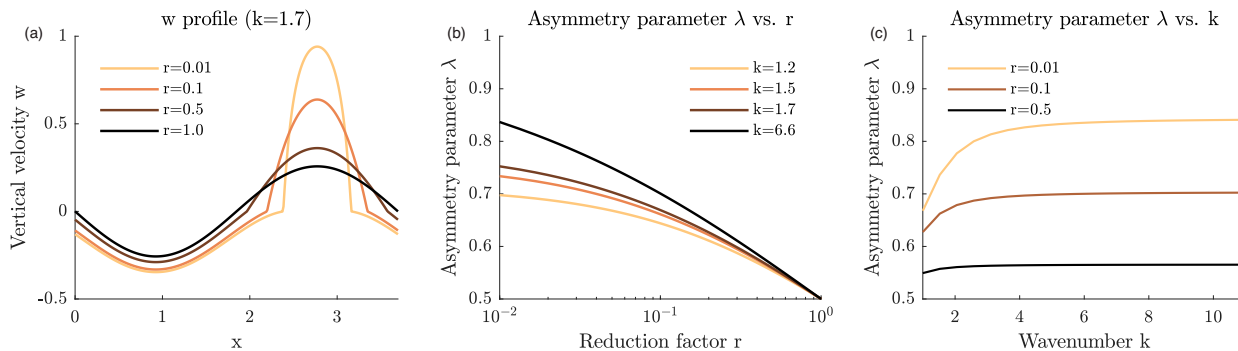
---

[4] Equations (14) and (15) have the property that for $r = 1$ and a given solution $w$ and Adv, there is also a solution $-w$ and $-$Adv, and thus, there is nothing to break the up–down symmetry and Adv must remain unskewed.

FIG. 6. (a) Vertical velocity profiles predicted by the 1D toy model at $k = 1.7$ for different values of $r$. (b) Asymmetry parameter $\lambda$ for the vertical velocity field predicted by the 1D toy model [Eq. (17)] for different wavenumbers $k$ as a function of the reduction factor $r$. (c) Asymmetry parameter $\lambda$ for the vertical velocity field predicted by the 1D toy model for different values of the reduction factor $r$ as a function of $k$.

moist omega equation is the same as that outlined in section 2a. For later comparison to the reduced stability GCM simulations, the typical wavenumber $k$ is estimated by calculating the centroid wavenumber of the 1D zonal $w$ power spectrum $P(k)$ at 500 hPa,

$$k_{\text{centroid}} = \frac{\sum\limits_{k'} k' P(k')}{\sum\limits_{k'} P(k')}, \qquad (18)$$

averaging $k_{\text{centroid}}$ across the latitude band 25°–65° and in time of the reduced-stability GCM simulation at $r = 0.01$. We non-dimensionalize the wavenumber by the deformation radius in pressure coordinates, $L_D = \sqrt{\sigma_{500}}\Delta p / (2\sqrt{2}f)$, where $\sigma_{500}$ is the static stability factor in pressure coordinates estimated from the reduced stability simulations at 500 hPa, and where $\Delta p = 800$ hPa and $f = 10^{-4}$ s$^{-1}$ were chosen as typical values for the troposphere depth and Coriolis parameter, respectively.[5] The power spectrum of $w$ has been used to calculate the centroid wavenumber because the asymmetry parameter will be most strongly affected by wavenumbers that dominate the vertical velocity field. We have also experimented with calculating $k$ directly from the centroid of the Adv spectrum. The two choices lead to very similar theoretical predictions of $\lambda$ for most values of $r$, as will be shown in Fig. 7 (solid vs dotted red line).

### 2) RESULTS

Vertical velocity profiles from the toy model are shown in Fig. 6a for a range of values of $r$ and for a fixed value of $k = 1.7$ which is the $k$ value that was diagnosed from the reduced stability GCM simulation at $r = 0.01$. Values of $\lambda$ as a function of both $r$ and $k$ are shown in Figs. 6b and 6c. Focusing on the vertical velocity profile at $k = 1.7$ (Fig. 6a), we see that although the ascent length shrinks as $r$ becomes smaller, the ascent length does not collapse and the vertical velocity

profiles do not become very asymmetric, especially compared to the profile of the mode predicted by 1D theory at $r = 0.1$ (Fig. 5a). Looking at the corresponding behavior of $\lambda(r)$ at $k = 1.7$ in Fig. 6b, we find that the toy model has a value of $\lambda = 0.75$ at $r = 0.01$ and asymptotes to $\lambda \simeq 0.78$ as $r \to 0$ (not shown). By comparison the 1D modal theory has a value of $\lambda = 0.95$ at $r = 0.01$ (Fig. 5b) and asymptotes to $\lambda = 1$ as $r \to 0$ (this limit is known from the theory of moist baroclinic modes, which predicts vanishing updraft length as $r \to 0$; Emanuel et al. 1987; Zurita-Gotor 2005). Thus, the asymmetries are much higher for modal theory than for the toy model.

In addition to predicting that $\lambda$ increases as $r$ decreases, the toy model also predicts that $\lambda$ increases with increasing wavenumber $k$, and the sensitivity to $k$ is greatest for low values of $r$ (Figs. 6b,c). When $r = 0.5$, for instance, the asymmetry is already converged at $k \approx 2$ but when $r = 0.01$ the asymmetry is converged only at $k \approx 6$. The dependence of $\lambda$ on $k$ can be understood by considering the left-hand side of the toy model Eq. (17). Increasing $k$ leads to smaller length scales and thus increases the importance of the first term on the left-hand side compared to the second term (because of the Laplacian operator in the first term), and it is the first term that is the root cause of asymmetry through $\mathcal{R}(\omega)$.

As shown in Fig. 7, the toy model prediction for $\lambda$ is in reasonably good agreement with the reduced stability GCM simulations given the simplicity of the toy model (solid red vs solid blue line). Very similar results are found when $k$ is calculated from the centroid of the Adv rather than $w$ spectrum (red dotted line in Fig. 7), even though $k$ is 1.7 times larger in this case averaged over all $r$ values and reaches values nearly twice as large at $r = 0.01$ ($k = 3.2$ instead of $k = 1.7$). This is because $\lambda$ from the toy model theory is not strongly sensitive to $k$ except for very low $r$ values (Fig. 6c). The underestimate of $\lambda$ as $r \to 1$ by the toy model is likely a result of the simplified nature of the dynamical forcing which is completely unskewed and represented by a simple sinusoid, since the full 3D moist QG omega inversion does a better job at reproducing the GCM asymmetry for $r \to 1$ (see dashed line in Fig. 7). The assumption of a one-dimensional dynamical forcing also contributes to underestimating $\lambda$: while the GCM vertical

---

[5] Note the extra factor of 2 in the definition of the deformation radius because $H$ in our two-layer theory is the layer height and not the tropopause height.
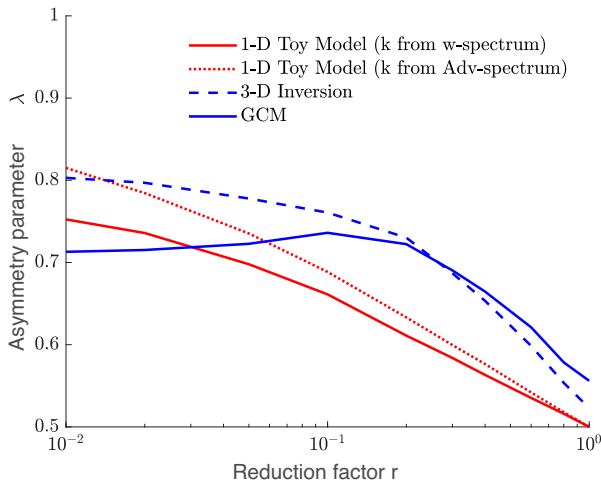
FIG. 7. Comparison of the asymmetry parameter $\lambda$ for the vertical velocity field predicted by the 1D toy model [Eq. (17); red lines], to the asymmetry found in the reduced-stability GCM simulation (blue solid line; as in Fig. 3a) and the 3D omega equation inversions applied to the reduced stability GCM simulations (blue dashed line, as in Fig. 3a). The red solid line shows the 1D toy model prediction using a wavenumber $k$ which was calculated from the centroid of the $w$ spectrum of the GCM simulation. The red dotted line shows the 1D toy model prediction where the wavenumber was alternatively calculated from the centroid of the Adv spectrum.

velocity fields include linear frontal bands, they are not purely one-dimensional, and including this two-dimensionality would increase the effective $k$ and thus increase $\lambda$. The overestimate of $\lambda$ at low $r$ values by the toy model points to a deficiency of the moist QG omega framework at capturing all the controls on the vertical velocity field, since the full 3D moist QG omega inversions also overestimate $\lambda$ at $r = 0.01$.

Overall, the toy model helps to explain why $\lambda$ increases less rapidly as $r$ decreases compared to moist baroclinic modes, and it also demonstrates a weak sensitivity of $\lambda$ to the wavenumber of the dynamical forcing in the QG omega equation.

## 4. Applying the toy model to the seasonal cycle of $\lambda$ in reanalysis

We next apply the toy model to the seasonal cycle of $\lambda$ observed in the current climate and contrast it with the predictions from moist baroclinic modes. The seasonal cycle forms a useful test ground for asymmetry theories, since the moist static stability is smaller in summer than in winter, particularly in the Northern Hemisphere. We compare the theoretical predictions from the 1D modal theory and the 1D toy model to the seasonal cycle of $\lambda$ found in ERA5 at 500 hPa in both the Northern Hemisphere (NH) and Southern Hemisphere (SH) (Fig. 8). We use ERA5 as a modern global reanalysis in which the dynamics were evolved at the highest available resolution, but earlier reanalyses can show quite different results as discussed in appendix B.

### a. Methods: Calculation of $\lambda$ and evaluation of theories based on reanalysis

The vertical velocity and temperature data used are 6-hourly fields spanning the latitude band 30°–70° and years 2009–18. The fields have been coarse grained from a native ERA5 grid spacing of 0.25° to 1.5° to make it more comparable to the GCM grid spacing (1.4°) and because the omega equation has been found to remain applicable only down to horizontal scales of roughly 140 km (Battalio and Dyer 2017). We show and discuss the results for $\lambda$ at the native ERA5 grid spacing in appendix B.

The asymmetry parameter $\lambda$ in reanalysis has been calculated based on a horizontal average over the latitude band and then averaged over the 10 years for each month. For the theoretical predictions, $r$ was calculated from the temperature field at 500 hPa using Eq. (6), and then averaged over the latitude band 30°–70° and over the 10 years for each month. The wavenumber $k$ was calculated again as the centroid wavenumber of the 1D zonal power spectrum of $w$ in ERA5 at 500 hPa using Eq. (18), and then averaged over the latitude band and over the 10-yr period for each month. Again, we have also tried estimating $k$ from the centroid of spectrum of Adv rather than the spectrum of $w$, but the toy model predictions were nearly identical, because $\lambda$ is not strongly sensitive to the choice of $k$ for the values of $r$ considered, and thus, these results are not shown. The wavenumber $k$ was then nondimensionalized by the deformation radius $L_D = \sqrt{\sigma_{500}}\Delta p/(2\sqrt{2}f)$, where $\sigma_{500}$ was averaged over the latitude band and over 10 years for each month, and $\Delta p = 800$ hPa and $f = 10^{-4}$ s$^{-1}$ were again chosen to reflect typical values of the tropopause depth and Coriolis parameter, respectively. Using the values of $r$ and $k$ for each month, the 1D toy model and the 1D modal theory (for which only $r$ is needed) were solved as described in section 3 to produce the theoretical predictions seen in Fig. 8.

### b. Seasonal cycle of $\lambda$

Looking at Fig. 8, we see that $\lambda$ in ERA5 has a seasonal cycle that peaks during summer in each hemisphere. This is as expected given that $r$ as shown in Fig. 9a decreases as the stratification becomes closer to moist adiabatic in summer (Stone and Carlson 1979), and it is also consistent with the result that $\lambda$ is larger in summer compared to winter in extratropical cyclones (Tamarin-Brodsky and Hadas 2019). The seasonal cycle is more pronounced in the NH, varying between values of $\lambda = 0.62$ and $\lambda = 0.69$, than in the SH where it varies between $\lambda = 0.62$ and $\lambda = 0.65$.

### c. Toy model versus modal prediction for the seasonal cycle

Given that $r$ undergoes large variations between winter and summer months ($0.10 < r < 0.45$ in the NH and $0.28 < r < 0.40$ in the SH) as shown in Fig. 9a, the magnitude of the seasonal cycle of $\lambda$ is surprisingly small in both hemispheres from the point of view of modal theory. Indeed, 1D modal theory consistently overestimates $\lambda$ in both hemispheres reaching peak values of $\lambda = 0.83$ in the NH and $\lambda = 0.74$ in the SH, and overestimates the size of the seasonal range of $\lambda$ by a factor of 2.6 in the NH and 2.4 in the SH. This is in line with the results
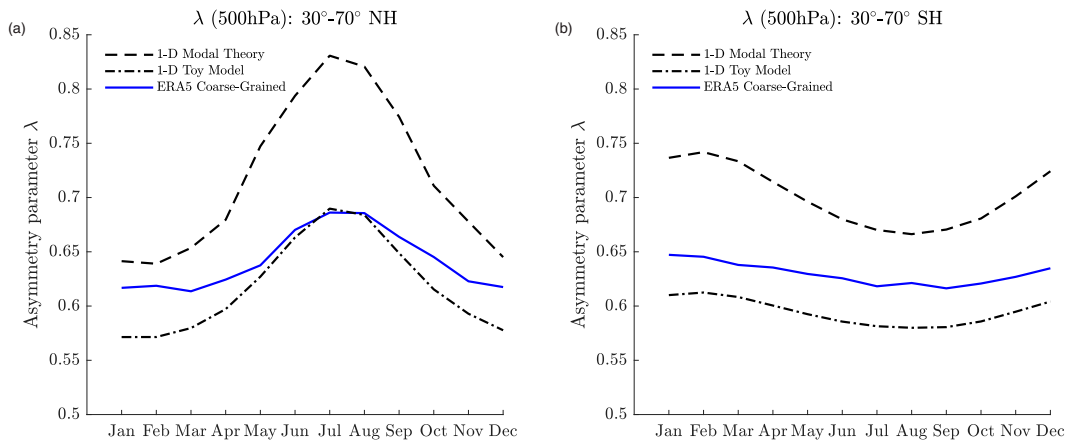
FIG. 8. (a) Comparison of the seasonal cycle of the asymmetry parameter $\lambda$ at 500 hPa in the Northern Hemisphere (NH) from ERA5 (blue line) to the predictions from the 1D toy model (black dash–dotted line) and 1D modal theory (black dashed line). Six-hourly fields were used for all reanalysis data spanning years 2009 to 2018. ERA5 fields were coarse grained from a native grid spacing of 0.25° to 1.5°. The asymmetry parameter has been calculated over the latitude band of 30°–70°. (b) As in (a), but for the Southern Hemisphere (SH).

of the idealized GCM simulations which showed that variations of $\lambda$ in the macroturbulent state with warming are considerably smaller than what moist modal theory predicts.

In comparison to the modal theory, the seasonal cycle range and overall values in reanalysis are better captured by the 1D toy model. The toy model still overestimates the size of the seasonal cycle by 1.6 in the NH and 1.1 in the SH, but these overestimates are considerably smaller than what was found from modal theory (2.6 and 2.4, respectively). According to the toy model, the seasonal cycle in $\lambda$ is primarily from the variations in $r$ because variations of $k$ (between 2.5 and 3.2 in the NH, and between 2.3 and 2.5 in the SH, see Fig. 9b) would only substantially affect $\lambda$ at smaller values of $r$ than are found in the seasonal cycle (compare the variations of $\lambda$ with $k$ predicted by the toy model at $r = 0.01$ and $r = 0.5$ in Fig. 6c). This was further checked by calculating $\lambda$ from the toy model keeping $k$ fixed over the seasonal cycle which did not affect the results in Fig. 8. This is also the reason why the

toy model predictions remain virtually unaffected when $k$ is taken from the centroid of the Adv spectrum rather than the $w$ spectrum. Hence, from the point of view of the toy model, it is the weak seasonality of $r$ in the SH that is reason for weak seasonality of $\lambda$ in SH and it is the stronger seasonality of $r$ in the NH that is the reason for a stronger seasonality of $\lambda$ in the NH.

In conclusion, despite the simplicity and rough approximations of the toy model, we argue that it better captures the moderate variation of $\lambda$ that is observed over the seasonal cycle as compared to modal theory.

## 5. Conclusions

Idealized GCM simulations of moist macroturbulence show that the asymmetry of the vertical velocity distribution is considerably smaller than what moist baroclinic instability theory predicts in warm climates or low values of $r$. This is significant given that the atmosphere is constantly in a state more akin to
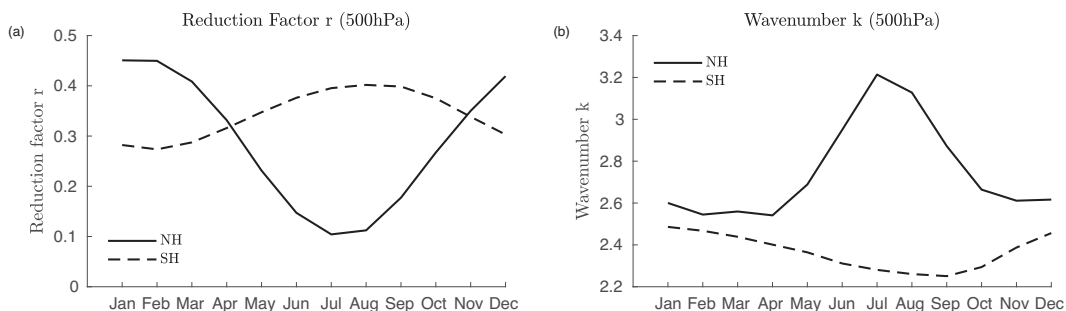


FIG. 9. Seasonal cycle of (a) the static stability reduction factor $r$ and (b) the nondimensional wavenumber of the dynamical forcing $k$ in the Northern (solid) and Southern (dashed) Hemispheres at 500 hPa in ERA5. ERA5 fields have been coarse grained from a native grid spacing of 0.25° to 1.5°. The reduction factor and wavenumber of the dynamical forcing have been averaged over latitudes 30°–70° and years 2009–18. $r = 1$ corresponds to a dry atmosphere, and $r = 0$ corresponds to a moist atmosphere with a moist adiabatic lapse rate. In both hemispheres, $r$ is smallest during the summer, but the seasonal cycle is more pronounced in the Northern Hemisphere.

that of the macroturbulent simulations than the moist baroclinic modes that our theoretical understanding is based on. This makes the development of a theory for the asymmetry in the macroturbulent state desirable.

To bridge this gap in understanding, we have applied inversions of a moist QG omega equation [Eq. (2)] to the idealized GCM output to identify why the asymmetry is larger in the modal compared to macroturbulent regime (section 2). The inversions showed that while dynamical forcing of the omega equation is very skewed in the modal regime, it contributes negligibly to the asymmetry in the macroturbulent regime which is almost entirely determined by the reduction in static stability in ascending air on the left-hand side of the moist omega equation (Fig. 3). Hence, the asymmetry in the macroturbulent regime of the simulations is lower than for the modes.

A two-layer moist QG framework was then used to understand asymmetry behavior (section 3). We showed that in the modal regime, a feedback between the dynamical forcing and the vertical velocity [deduced from Eqs. (14) and (15)] leads to large asymmetries contributed by the dynamical forcing, consistent with what was found for the modes in the GCM. Such a feedback is not expected for the macroturbulent phase because of advective nonlinearities which disrupt the modal structure and lower the skewness of the dynamical forcing of the moist omega equation.

We then distilled the insights from the moist omega inversions and, in particular, the unskewed dynamical forcing in the macroturbulent regime into a simple 1D toy model of the moist QG omega equation by replacing Adv by an unskewed function [Eq. (17)]. The toy model was solved for a given wavenumber $k$ of the dynamical forcing on the right-hand side of the omega equation and for a given static stability reduction factor $r$. Compared to the 1D moist modal theory, the toy model was able to better reproduce the weak increase of the asymmetry with warming that has been observed in the macroturbulent regime of the idealized GCM simulations (Figs. 6, 7). However, both toy model and the full 3D moist QG omega equation inversions overpredict the asymmetry found in the idealized GCM simulations in warm climates or at low values of the reduction factor $r$ pointing to a deficiency of the moist QG omega framework at capturing all the controls on $\lambda$ in these limits.

We went on to study the seasonal cycle of $\lambda$ in reanalysis which forms a useful test ground for asymmetry theories, since the moist static stability varies a lot between seasons, particularly in the NH (section 4). We showed that moist baroclinic modal theory considerably overpredicts the increase in $\lambda$ from winter to summer, whereas the toy model better reproduces $\lambda$ over the seasonal cycle in ERA5 (Fig. 8). The interpretation is once again that asymmetry changes in macroturbulent flows in response to changes in moist static stability are much smaller than what moist unstable baroclinic modes suggest. While the seasonal cycle of $\lambda$ is somewhat similar in ERA5 and the earlier ERAI, it is completely absent in the NCEP2 reanalysis (appendix B), and further studies of the sensitivity of $\lambda$ to resolution and reanalysis product would be useful.

The dynamical forcing assumed in the toy model is highly idealized, but we argue that it is nonetheless useful to illustrate the controls on the asymmetry implied by the moist QG omega equation. Our toy model theory is not closed since it takes as given a single wavenumber for the dynamical forcing, although

the sensitivity to this wavenumber is relatively weak. A more complete theory would not use just one wavenumber but rather take as input the power spectrum of the dynamical forcing, and understanding what sets this power spectrum remains an important outstanding problem for future work.

Finally, our toy model predicts that high $\lambda$ is still possible in a macroturbulent state even with unskewed dynamical forcing of the omega equation provided that 1) $r$ is sufficiently low, 2) $k$ is large meaning that the length scale of the dynamical forcing is small compared to the dry deformation radius, and 3) the Rossby number is low so that the omega equation remains valid despite the high $k$ and low $r$. It would thus be interesting to investigate such states and their asymmetries further by running simulations of the two-layer moist QG systems and comparing them to simulations of the moist primitive equations at a range of Rossby numbers, and we plan to report results on this in future work.

## APPENDIX A

### Derivation of the Moist QG Omega Equation

We start from the omega equation with external heating,

$$\nabla^2(\sigma\omega) + f_0^2 \omega_{pp} = \text{Adv} - \frac{\kappa}{p}\nabla^2 J, \quad (A1)$$

where $J$ is the diabatic heating and $\kappa$ is the ratio of $R$ to the specific heat capacity at constant pressure $c_p$ (Li and O'Gorman 2020). In the reduced stability formulation, the thermodynamic equation is given by

$$T_t + uT_x + vT_y - \mathcal{R}(\omega)S_p\omega = 0, \quad (A2)$$

where $S_p = -(T/\theta)\theta_p$. Rearranging the thermodynamic equation to make the heating term explicit, we obtain

$$T_t + uT_x + vT_y - S_p\omega = -[1 - \mathcal{R}(\omega)]S_p\omega = \frac{J}{c_p}, \quad (A3)$$

from which it follows that

$$J = -[1 - \mathcal{R}(\omega)]c_p S_p\omega = -\frac{p}{\kappa}[1 - \mathcal{R}(\omega)]\sigma\omega, \quad (A4)$$

where we have used the relation $c_p S_p = (p/\kappa)\sigma$ to obtain the second equality. Plugging this expression for $J$ into Eq. (A1)

and combining the heating term on the right-hand side with the static stability term on the left-hand side of Eq. (A1), we obtain the moist omega equation [Eq. (2)] in the text in which the effects of latent heating are now represented as an internal process.

## APPENDIX B

### Discussion of Differences in λ for Different Reanalysis Products and Resolutions

We compare the seasonal cycle of λ based on different reanalysis products and with and without coarse graining of ω. Figure B1 shows results for ERA5 data coarse grained to a grid spacing of 1.5° as was used in our main analysis, ERA5 data at their native grid spacing of 0.25°, ERAI data which have grid spacing of 0.75° (Dee et al. 2011), and NCEP2 reanalysis which has a grid spacing of 2.5° (Kanamitsu et al. 2002). The coarse graining we applied to ERA5 can be seen to have modestly decreased λ with the biggest effect in NH summer. Comparing ERA5, ERAI, and NCEP2 on their native grids, we find that the lower-resolution ERAI has somewhat smaller values of λ than ERA5 but overall remains quite similar, whereas NCEP2 shows much smaller values and almost no seasonal cycle. This is true despite the fact that the seasonal

cycle of r is close to identical in all reanalysis products (not shown) and follows the profile shown in Fig. 9a. The centroid wavenumber k is lower for NCEP2 than for the other reanalyses but we find this is not sufficient to explain the absence of a seasonal cycle according to the toy model. The absence of a seasonal cycle in NCEP2 is also not just due to the resolution of ω: a seasonal cycle for ERA5 persists even when it is coarse grained to the 2.5° grid spacing of NCEP2 (not shown). Similarly, we observe that λ for ERA5 coarse grained to 1.5° is larger than what is found from ERAI despite the fact that the ERAI grid spacing is 0.75°. This suggests that the differences in λ between reanalysis products are not just a result of the resolution of ω but are also affected by the different dynamics and other aspects of the models.

The question arises whether future reanalysis products with substantially higher resolution than ERA5 could show an even larger seasonal cycle of λ. We do not anticipate this to be the case because Booth et al. (2015) found that vertically averaged λ did not increase from a grid spacing of 50 to 3.125 km in simulations of a moist baroclinic life cycle, and λ at z = 5 km only increased slightly over this range of grid spacings. The QG omega equation is not a good tool to use at such short length scales, and it will be interesting to analyze the question of λ at very high resolution using other theoretical approaches in future work.
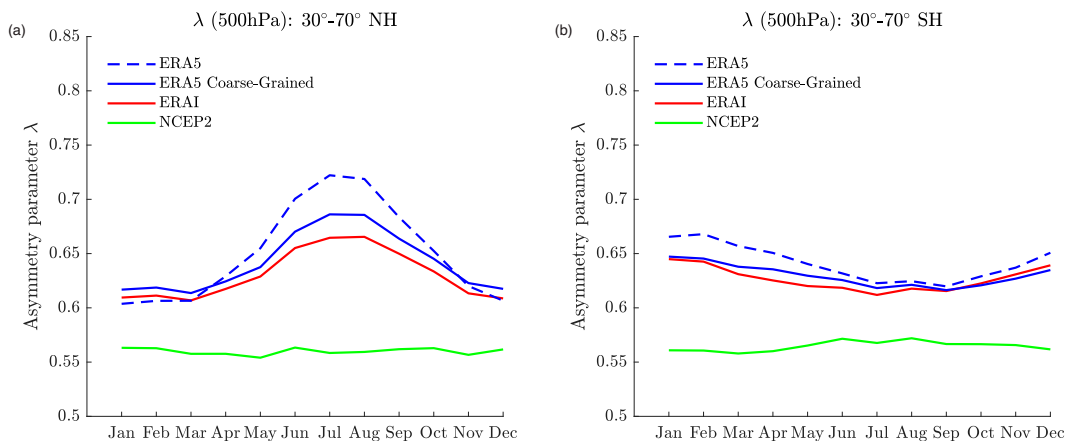


FIG. B1. (a) Seasonal cycle of the asymmetry parameter λ at 500 hPa in the NH in ERA5 with grid spacing of 0.25° (dashed blue line), in ERA5 coarse grained to a grid spacing of 1.5° (blue solid line), in ERAI with grid spacing of 0.75° (red solid line), and in NCEP2 reanalysis which has a grid spacing of 2.5° (green solid line). The 6-hourly fields were used for all reanalysis data spanning the years 2009–18 and a latitude band 30°–70°. (b) As in (a), but for the SH.

## REFERENCES

Battalio, M., and J. Dyer, 2017: The minimum length scale for evaluating QG omega using high-resolution model data. *Mon. Wea. Rev.*, **145**, 1659–1678, https://doi.org/10.1175/MWR-D-16-0241.1.

Booth, J. F., L. Polvani, P. A. O'Gorman, and S. Wang, 2015: Effective stability in a moist baroclinic wave. *Atmos. Sci. Lett.*, **16**, 56–62, https://doi.org/10.1002/asl2.520.

Dee, D. P., and Coauthors, 2011: The ERA-Interim reanalysis: Configuration and performance of the data assimilation

system. *Quart. J. Roy. Meteor. Soc.*, **137**, 553–597, https://doi.org/10.1002/qj.828.

Dwyer, J. G., and P. A. O'Gorman, 2017: Moist formulations of the Eliassen–Palm flux and their connection to the surface westerlies. *J. Atmos. Sci.*, **74**, 513–530, https://doi.org/10.1175/JAS-D-16-0111.1.

Emanuel, K. A., M. Fantini, and A. J. Thorpe, 1987: Baroclinic instability in an environment of small stability to slantwise moist convection. Part I: Two-dimensional models. *J. Atmos. Sci.*, **44**, 1559–1573, https://doi.org/10.1175/1520-0469(1987)044<1559:BIIAEO>2.0.CO;2.

Fantini, M., 1995: Moist Eady waves in a quasigeostrophic three-dimensional model. *J. Atmos. Sci.*, **52**, 2473–2485, https://doi.org/10.1175/1520-0469(1995)052<2473:MEWIAQ>2.0.CO;2.

Ferziger, J. H., and M. Perić, 2002: *Computational Methods for Fluid Dynamics*. 3rd ed. Springer, 426 pp., https://doi.org/10.1007/978-3-642-56026-2.

Frierson, D. M. W., 2007: The dynamics of idealized convection schemes and their effect on the zonally averaged tropical circulation. *J. Atmos. Sci.*, **64**, 1959–1976, https://doi.org/10.1175/JAS3935.1.

——, I. M. Held, and P. Zurita-Gotor, 2006: A gray-radiation aquaplanet moist GCM. Part I: Static stability and eddy scale. *J. Atmos. Sci.*, **63**, 2548–2566, https://doi.org/10.1175/JAS3753.1.

Held, I. M., 1999: The macroturbulence of the troposphere. *Tellus*, **51B**, 59–70, https://doi.org/10.3402/tellusb.v51i1.16260.

Holton, J. R., 2004: *An Introduction to Dynamic Meteorology*. 4th ed. Academic Press, 535 pp.

Kanamitsu, M., W. Ebisuzaki, J. Woollen, S.-K. Yang, J. J. Hnilo, M. Fiorino, and G. L. Potter, 2002: NCEP–DOE AMIP-II reanalysis (R-2). *Bull. Amer. Meteor. Soc.*, **83**, 1631–1644, https://doi.org/10.1175/BAMS-83-11-1631.

Kohl, M., and P. A. O'Gorman, 2022: The diabatic Rossby vortex: Growth rate, length scale, and the wave–vortex transition. *J. Atmos. Sci.*, **79**, 2739–2755, https://doi.org/10.1175/JAS-D-22-0022.1.

Levine, X. J., and T. Schneider, 2015: Baroclinic eddies and the extent of the Hadley circulation: An idealized GCM study. *J. Atmos. Sci.*, **72**, 2744–2761, https://doi.org/10.1175/JAS-D-14-0152.1.

Li, Z., and P. A. O'Gorman, 2020: Response of vertical velocities in extratropical precipitation extremes to climate change. *J. Climate*, **33**, 7125–7139, https://doi.org/10.1175/JCLI-D-19-0766.1.

Nielsen-Gammon, J. W., and D. A. Gold, 2008: Dynamical diagnosis: A comparison of quasigeostrophy and Ertel potential vorticity. *Synoptic-Dynamic Meteorology and Weather Analysis and Forecasting, Meteor. Monogr.*, No. 33, Amer. Meteor. Soc., 183–202, https://doi.org/10.1175/0065-9401-33.55.183.

O'Gorman, P. A., 2011: The effective static stability experienced by eddies in a moist atmosphere. *J. Atmos. Sci.*, **68**, 75–90, https://doi.org/10.1175/2010JAS3537.1.

——, and T. Schneider, 2008: The hydrological cycle over a wide range of climates simulated with an idealized GCM. *J. Climate*, **21**, 3815–3832, https://doi.org/10.1175/2007JCLI2065.1.

——, T. M. Merlis, and M. S. Singh, 2018: Increase in the skewness of extratropical vertical velocities with climate warming: Fully nonlinear simulations versus moist baroclinic instability. *Quart. J. Roy. Meteor. Soc.*, **144**, 208–217, https://doi.org/10.1002/qj.3195.

Pendergrass, A. G., and E. P. Gerber, 2016: The rain is askew: Two idealized models relating the vertical velocity and precipitation distributions in a warming world. *J. Climate*, **29**, 6445–6462, https://doi.org/10.1175/JCLI-D-16-0097.1.

Perron, M., and P. Sura, 2013: Climatology of non-Gaussian atmospheric statistics. *J. Climate*, **26**, 1063–1083, https://doi.org/10.1175/JCLI-D-11-00504.1.

Pfahl, S., P. A. O'Gorman, and M. S. Singh, 2015: Extratropical cyclones in idealized simulations of changed climates. *J. Climate*, **28**, 9373–9392, https://doi.org/10.1175/JCLI-D-14-00816.1.

Sardeshmukh, P. D., G. P. Compo, and C. Penland, 2015: Need for caution in interpreting extreme weather statistics. *J. Climate*, **28**, 9166–9187, https://doi.org/10.1175/JCLI-D-15-0020.1.

Stone, H. L., 1968: Iterative solution of implicit approximations of multidimensional partial differential equations. *SIAM J. Numer. Anal.*, **5**, 530–558, https://doi.org/10.1137/0705044.

Stone, P. H., and J. H. Carlson, 1979: Atmospheric lapse rate regimes and their parameterization. *J. Atmos. Sci.*, **36**, 415–423, https://doi.org/10.1175/1520-0469(1979)036<0415:ALRRAT>2.0.CO;2.

Tamarin-Brodsky, T., and O. Hadas, 2019: The asymmetry of vertical velocity in current and future climate. *Geophys. Res. Lett.*, **46**, 374–382, https://doi.org/10.1029/2018GL080363.

Whitaker, J. S., and C. A. Davis, 1994: Cyclogenesis in a saturated environment. *J. Atmos. Sci.*, **51**, 889–908, https://doi.org/10.1175/1520-0469(1994)051<0889:ciase>2.0.co;2.

Zedan, M., and G. E. Schneider, 1983: A three-dimensional modified strongly implicit procedure for heat conduction. *AIAA J.*, **21**, 295–303, https://doi.org/10.2514/3.8068.

Zurita-Gotor, P., 2005: Updraft/downdraft constraints for moist baroclinic modes and their implications for the short-wave cutoff and maximum growth rate. *J. Atmos. Sci.*, **62**, 4450–4458, https://doi.org/10.1175/JAS3630.1.